International Journal of Minerals, Metallurgy and Materials
Volume 29, Number 2, February 2022, Page 283
https://doi.org/10.1007/s12613-021-2316-0

Effects of the incorporation amounts of CdS and $Cd(SCN_2H_4)_2Cl_2$ on the performance of perovskite solar cells

Jihong Zheng[1),*], *Liangxin Zhu*[1),*], *Zhitao Shen*[1)], *Fumin Li*[1)], *Lanyu Ling*[2),✉], *Huilin Li*[1),✉], *and Chong Chen*[1),✉]

1) Henan Key Laboratory of Photovoltaic Materials, Henan University, Kaifeng 475004, China
2) School of Physics and Electronics, Henan University, Kaifeng 475004, China
(Received: 13 April 2021; revised: 10 June 2021; accepted: 11 June 2021)

Abstract: An excellent organolead halide perovskite film is important for the good performance of perovskite solar cells (PSCs). However, defects in perovskite crystals can affect the photovoltaic properties and stability of solar cells. To solve this problem, this study incorporated a complex of CdS and $Cd(SCN_2H_4)_2Cl_2$ into the $CH_3NH_3PbI_3$ active layer. The effects of different doping concentrations of CdS and $Cd(SCN_2H_4)_2Cl_2$ on the performance and stability of PSCs were analyzed. Results showed that doping appropriate incorporation concentrations of CdS and $Cd(SCN_2H_4)_2Cl_2$ in $CH_3NH_3PbI_3$ can improve the performance of the prepared solar cells. In specific, CdS and $Cd(SCN_2H_4)_2Cl_2$ can effectively passivate the defects in perovskite crystals, thereby suppressing the charge recombination in PSCs and promoting the charge extraction at the TiO_2/perovskite interface. Due to the reduction of perovskite crystal defects and the enhancement of compactness of the CdS:$Cd(SCN_2H_4)_2Cl_2$:$CH_3NH_3PbI_3$ composite film, the stability of PSCs is significantly improved.

Keywords: perovskite solar cells; charge extraction; defect passivation; incorporation concentration

1. Introduction

In recent years, perovskite solar cells (PSCs) based on lead trihalide perovskite materials (ABX_3, $A = CH_3NH_3^+$; $B = Pb^{2+}$; $X = I^-$, Cl^-, Br^-) have attracted extensive attention because of their simple fabrication, low cost [1−2], and high power conversion efficiency (PCE) [3−5] The PCE of PSCs has been increased from 3.8% to 25.5% [6−7] by using a mixed anion/cation perovskite absorber [8]. This rapid progress is mainly related to the high light absorption coefficient, high carrier mobility, and long carrier diffusion length of perovskite materials [9−10]. The structure of PSCs can be divided into two types, namely, mesoporous scaffold and planar heterojunction architectures [11−12]. Compared with that in the planar architecture, the charge extraction in the mesoporous architecture is more effective because of the larger contact area between the mesoporous layer and perovskite film [11]. In general, the PSCs are mainly composed of five parts, namely, indium-doped tin oxide (ITO)/fluorine-doped tin oxide (FTO) substrate, electron transport layer (ETL), hole transport layer (HTL), perovskite layer, and Ag/Au pole, in which the perovskite film is important in the performance of the cells [13−15]. The most common perovskite film in PSCs is a polycrystalline film [16]. However, it has several defects at the grain boundaries and interfaces [17−19]. These defects decrease the quality of the perovskite film and further affect the separation and extraction of carriers. So far, high efficiency has been realized by two main approaches: effective coating and composition engineering, such as metal ion dopant [20], organic material insertion [21−22], and bi-layer strategies [23−24], which have improved the quality of perovskite films [25−26]. Recently, a strategy that combines chemical *in situ* synthesis and an anti-solvent process has been demonstrated. This strategy involves the incorporation of CdS and complex [$Cd(SCN_2H_4)_2Cl_2$] [27] into the $CH_3NH_3PbI_3$ layer by spin-coating the $CH_3NH_3PbI_3$ precursor with cadmium chloride hydrate ($2(CdCl_2)\cdot 5(H_2O)$) and thiourea onto the mp-TiO_2 surface. The incorporation of CdS and $Cd(SCN_2H_4)_2Cl_2$ into $CH_3NH_3PbI_3$ not only significantly improves the quality of the $CH_3NH_3PbI_3$ film and thus reduces the trap state density [28] in the perovskite layer but also promotes the charge transfer and maintains the stability of as-PSCs [27,29]. However, the most critical mechanisms for understanding these PSCs remain unclear. Thus, understanding the effect of different CdS:$Cd(SCN_2H_4)_2Cl_2$ incorporation amounts in the CdS:$Cd(SCN_2H_4)_2Cl_2$:$CH_3NH_3PbI_3$ (denoted as C:C:$CH_3NH_3PbI_3$) film on the performance of the newly developed C:C:$CH_3NH_3PbI_3$ bulk-heterojunction PSCs is important.

In this study, we systematically investigated the influence

*These authors contributed equally to this work.

✉ Corresponding authors: Lanyu Ling E-mail: 10110131@henu.edu.cn; Huilin Li E-mail: leehl@vip.henu.edu.cn; Chong Chen E-mail: chongchen@henu.edu.cn

of the incorporation amounts of CdS and $Cd(SCN_2H_4)_2Cl_2$ on the performance of PSCs and the underlying mechanism. Scanning electron microscopy (SEM) and photoluminescence (PL) spectra were used to investigate the effects of CdS and $Cd(SCN_2H_4)_2Cl_2$ on the morphology and photoelectric properties of the C:C:$CH_3NH_3PbI_3$ composite film. The electrochemical impedance spectra were used to study the dynamics of photogenerated charge transport and collection in the devices. The effects of different concentrations of CdS and $Cd(SCN_2H_4)_2Cl_2$ on the density and passivation mechanism of defect states were also studied. After concentration optimization, the efficiency of the PSCs based on the C:C:$CH_3NH_3PbI_3$ composite film reached 20.10%, which is 1.16 times that (17.31%) of the PSCs based on pure $CH_3NH_3PbI_3$ film, and the stability was also significantly enhanced.

2. Experimental

2.1. Materials and preparation of the precursor solution

Methylammonium iodide (MAI, ≥99.5%) and lead iodide (PbI_2, ≥99.9%) were ordered from Xi'an Polymer Light Technology Corp. China. Chlorobenzene (OCB, 99.5%), titanium butoxide (≥99.0%), acetylacetone (≥99.5%), cadmium chloride ($CdCl_2$, 99%), and bis(trifluoromethylsulfonyl)-imide lithium salt (Li-TFSI) (99%) were purchased from Shanghai Aladdin Biochemical Technology Co., Ltd., China. $2(CdCl_2)\cdot5(H_2O)$ was formed by disposing of $CdCl_2$ in the air for adequate moisture absorption, and thiourea ($CS(NH_2)_2$, 99%) was purchased from Sinopharm Chemical Reagent Beijing Co., Ltd., China without further treatment. 4-tert-butylpyridine (96%) was purchased from Sigma-Aldrich, USA. Spiro-OMeTAD (>99%) was purchased from Xi'an Polymer Light Technology Corp, China.

The compact TiO_2 (cp-TiO_2) precursor was synthesized as follows. Titanium tetraisobutanolate (1 mL), glacial acetic acid (1 mL), and acetaldehyde acetonide (1 mL) were added into the absolute ethanol solution (9 mL) gradually at room temperature with stirring for 2 h. Then, 1 mL of deionized water was slowly added into the above solution, and the obtained solution was stirred for 1 d to obtain an orange sol. The mesoporous TiO_2 (mp-TiO_2) precursor was compounded by mixing TiO_2 paste (Dyesol 18NR-T) and anhydrous ethanol at 1:7 by weight. The pure perovskite precursor was prepared by 1 M MAI ($CH_3NH_3PbI_3$) and 1 M PbI_2(1:1 in molar ratio) in N,N-dimethylformamide solution. Different concentrations of $CdCl_2$ and thiourea in a molar ratio of 1:3 were added to the pure $CH_3NH_3PbI_3$ precursor to prepare the C:C:$CH_3NH_3PbI_3$ precursor solution. In this study, a series of C:C:$CH_3NH_3PbI_3$ precursor solutions was obtained, and the molar concentrations of $CdCl_2$ were fixed at 0.01, 0.03, and 0.06 mM. Correspondingly, the prepared perovskite film with CdS (x) doped was denoted as FTO/cp-TiO_2/mp-TiO_2/C:C:$CH_3NH_3PbI_3$:CdS (x) (x = 0.01, 0.03, and 0.06 mM). The metal complex of CdS and $Cd(SCN_2H_4)_2Cl_2$ was synthesized by the following reaction:

$$2CS(NH_2)_2 + CdCl_2 \rightarrow Cd(SCN_2H_4)_2Cl_2;$$

$$2Cd(SCN_2H_4)_2Cl_2 \rightarrow CdS + NH_4CdCl_3 + 2NH_3 + HCl + CS_2 + HNCS + 2H_2NCN.$$

Then, 72.3 mg of spiro-OMeTAD, 29 μL of 4-tert-butylpyridine solution, and 18 μL of Li-TFSI solution (520 $mg\cdot mL^{-1}$ in acetonitrile) were dissolved into 1 mL of chlorobenzene to obtain the HTL precursor complex solution.

2.2. Fabrication of solar cells

The FTO substrates were cleaned with deionized water and isopropanol and dried with a Termovap sample concentrator. The substrates were cleaned by ultra-violet (UV) ozone for 15 min before depositing the compact TiO_2 layer. The prepared TiO_2 sol–gel solution was spin-coated onto clean FTO glasses at 6500 r/min for 30 s, and then the films were heated at 500°C for 30 min to obtain 40 nm-thick cp-TiO_2 films. A thick TiO_2 layer was formed by spin-coating TiO_2 nano-dispersion onto the FTO/cp-TiO_2 films at 3000 r/min for 30 s, and then the mp-TiO_2 films were heated at 500°C for 30 min to obtain FTO/cp-TiO_2/mp-TiO_2 films. The perovskite precursor was spin-coated onto the FTO/cp-TiO_2/mp-TiO_2 films at 4000 r/min for 30 s to obtain $CH_3NH_3PbI_3$ and C:C:$CH_3NH_3PbI_3$ perovskite layers. After the first 10 s of spin-coating, the ethyl ether solution was quickly dropped onto the mp-TiO_2 film. The perovskite films were then dried at 100°C for 10 min. For the HTL layer, a pre-prepared spiro-OMeTAD solution with additives of Li-TFSI and TBP was spin-coated onto the FTO/cp-TiO_2/mp-TiO_2/C:C:$CH_3NH_3PbI_3$ films at 4500 r/min for 30 s. Finally, the counter electrode of 80 nm-thick Au was thermally evaporated. The active area of the devices was 0.04 cm^2. The device structure and energy level alignment are shown in Fig. 1(a) and (b), re-

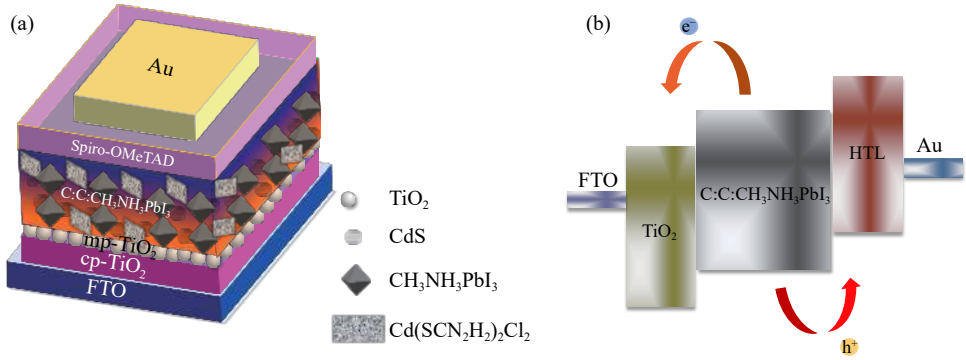

Fig. 1. (a) Schematic of the device structure and (b) energy level diagram of the device.

spectively.

2.3. Device characterization

The surface morphology and cross-sectional SEM images of the as-prepared films were measured by an SEM (JSM-7001F, Japan Electron Optics Laboratory Co., Japan) instrument. Time-resolved PL (TRPL) decay dynamics was measured using A HORIBA Jobin Yvon Fluorolog-3 spectrofluorometer system with a Xe 900 (450 W xenon arc lamp) as the light source, and an Edinburgh Instrument FLS 980 PL spectrometer was used to detect TRPL decay dynamics. The excitation source was a picosecond pulsed diode laser at 515 nm. The incident photon-to-electron conversion efficiency (IPCE) spectra were recorded using a solar cell quantum efficiency test system (Qtest Station 500ADX, United States dawn Technology Co., Ltd., USA). The current density–voltage (J–V) characteristics were measured using a computer-programmed Keithley 2400 source/meter, and the light source was standard AM 1.5G illumination at 100 $mW \cdot cm^{-2}$ with a Newport 94043A solar simulator. The forward scan (FS) (from – 1.2 to 0.2 V) and reverse scan (RS) (from 0.2 to −1.2 V) with a scanning rate of 20 $mV \cdot s^{-1}$ were scanned to obtain the J–V curves. The light intensity corrected by a standard silicon solar cell of the solar simulator was 100 $mW \cdot cm^{-2}$. All J–V curves of the as-prepared solar cells were performed in an ambient atmosphere (40%–50% relative humidity (RH)) at room temperature without encapsulation. Electrochemical impedance spectroscopy (EIS) of the fabricated cells was performed using a CHI660E (Chenhua Device Company, Shanghai, China) electrochemical measured system under ambient atmosphere (40%–50% RH), AM 1.5G illumination (100 $mW \cdot cm^{-2}$). The frequencies ranged from 100 mHz to 1 MHz. The resultant impedance spectra were simulated using the Z-view software.

2.4. Calculations

Electronic structure calculations were performed with the density functional theory as implemented in the Vienna *ab initio* simulation package [30−31], employing projected augmented wave potentials to describe the atomic core electrons and a plane wave basis set with a kinetic energy cutoff of 480 eV to expand the Kohn−Sham electronic states. For the exchange and correlation functional, the generalized gradient approximation in the Perdew–Burke–Ernzerhof format was used [32].

The $Cd(SCN_2H_4)_2Cl_2/CH_3NH_3PbI_3$ interface was simulated using a periodic slab model. That is, the single $Cd(SCN_2H_4)_2Cl_2$ molecule was adsorbed on the $CH_3NH_3PbI_3$ (001) surface (1.752 nm × 1.752 nm) with five atomic layers, and a vacuum thickness of 1.5 nm was added along the z direction. A 2 × 2 × 1 k-point mesh generated by Monkhorst–Pack scheme [33] was used to sample the Brillouin zone. The DFT-D2 method proposed by Grimme [34] was adopted to include van der Waals interactions. During structural optimization, all the atoms were fully relaxed until the atomic forces were smaller than 0.5 $eV \cdot nm^{-1}$. After the structure relaxation, static calculations were performed to obtain the electronic densities, which were converged to below 10^{-6} eV. The crystal structures and electronic densities were visualized by virtue of the VESTA [35] codes.

3. Results and discussion

SEM measurements were conducted to characterize the surface morphology and the structure of the as-prepared films. Fig. 2(a)–(d) show the typical top view SEM images of the prepared FTO/cp-TiO_2/mp-TiO_2/C:C:$CH_3NH_3PbI_3$ (x) films with x = 0, 0.01, 0.03, and 0.06 mM, respectively. As the concentrations of CdS and $Cd(SCN_2H_4)_2Cl_2$ were increased, the surface of the C:C:$CH_3NH_3PbI_3$ (x) film became more compact, and the size of the perovskite crystals became larger. Cross-sectional SEM images of the FTO/cp-TiO_2/mp-TiO_2/C:C:$CH_3NH_3PbI_3$ (x) (x = 0, 0.01, 0.03, and 0.06 mM) films were obtained, as shown in Fig. 2(e), to investigate the effects of CdS and $Cd(SCN_2H_4)_2Cl_2$ on the thickness of the FTO/cp-TiO_2/mp-TiO_2/C:C:$CH_3NH_3PbI_3$ film. The measured thicknesses of the cp-TiO_2, mp-TiO_2, and perovskite layers in these three films with different concentrations were approximately 50, 250, and 300 nm, respectively. Therefore, CdS and $Cd(SCN_2H_4)_2Cl_2$ exerted a minimal effect on the thicknesses of these three films [36]. Furthermore, Fig. 2(e) shows that the C:C:$CH_3NH_3PbI_3$ layer became more compact and uniform as the amounts of CdS and $Cd(SCN_2H_4)_2Cl_2$ were increased, which agrees with the results in Fig. 2 (a)–(d).

Steady-state PL spectra and TRPL decay transients were measured to explore the effects of CdS and $Cd(SCN_2H_4)_2Cl_2$ on the carrier transfer at the TiO_2/C:C:$CH_3NH_3PbI_3$ interface. The results are shown in Fig. 3(a) and (b), respectively. An excitation wavelength of 515 nm was used, as we reported previously [37−38]. Fig. 3(a) shows that all the samples showed a strong PL peak around 772 nm, which is in accordance with the applied $CH_3NH_3PbI_3$ absorber [2,39]. Moreover, as more CdS and $Cd(SCN_2H_4)_2Cl_2$ were incorporated, the PL intensities initially decreased and then increased. These results can be explained as follows. First, the $CH_3NH_3PbI_3$/CdS and $CH_3NH_3PbI_3$/$Cd(SCN_2H_4)_2Cl_2$ interface formed with increasing doping concentration, which was conducive to the photogenerated charge transfer from the perovskite to CdS and $Cd(SCN_2H_4)_2Cl_2$. Second, the charge remaining in the perovskite crystals was transferred to ETL or HTL through the continuous channel formed by the perovskite crystals, thus reducing the PL intensity [40], which was consistent with previous results [36]. However, when the concentration of doped complex was excessively high, the contact between perovskite crystals became worse or even blocked by the complex. Thus, the photogenerated charges in the perovskite crystals cannot be effectively transferred to the ETL or HTL, which increased the probability of charge recombination and the PL intensity. The time-resolved PL decay transients were detected at 775 nm to analyze the fundamental photoinduced charge extract and transfer process quantitatively [37], and the results are shown in Fig. 3(b). By fitting the experimental

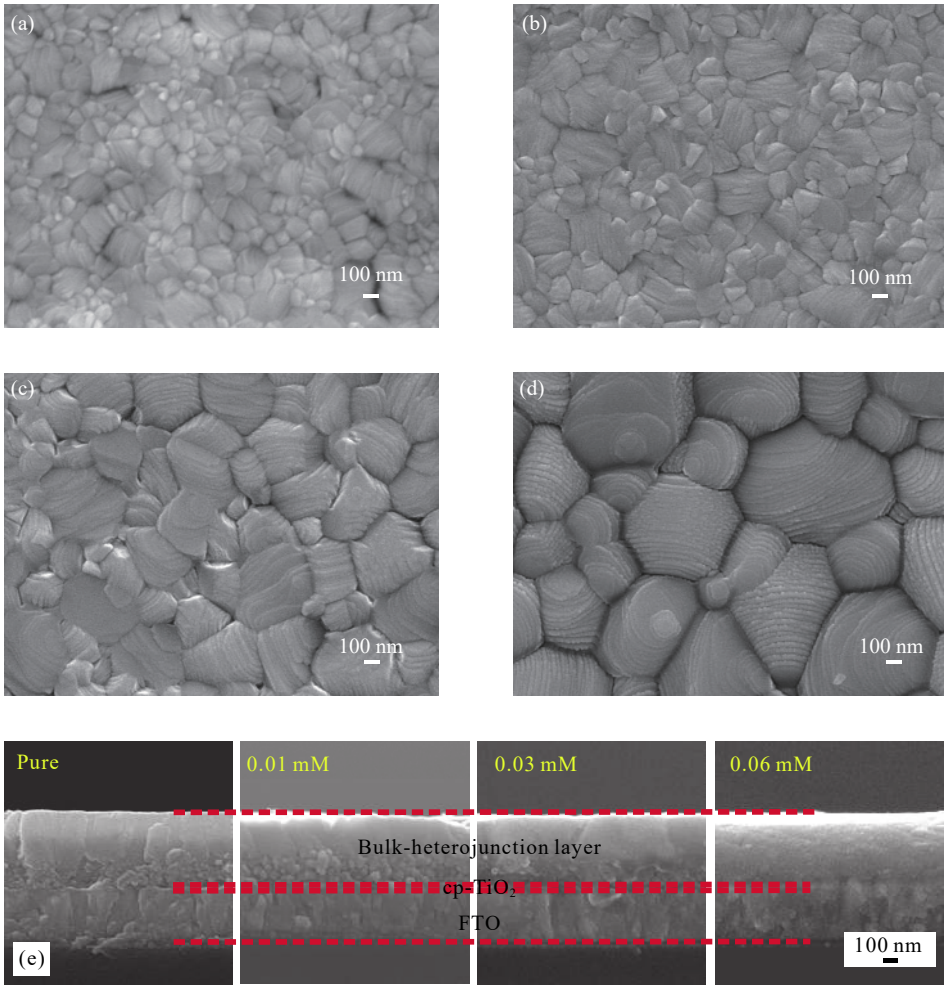

Fig. 2. SEM images showing the top view of (a) FTO/cp-TiO_2/mp-TiO_2/$CH_3NH_3PbI_3$, FTO/cp-TiO_2/mp-TiO_2/C:C:$CH_3NH_3PbI_3$ (x) films for (b) x = 0.01 mM, (c) x = 0.03 mM, and (d) x = 0.06 mM. (e) Cross-sectional SEM images of the FTO/cp-TiO_2/mp-TiO_2/C:C:$CH_3NH_3PbI_3$ film.

results, the carrier lifetime τ values of the films with x = 0.01, 0.03, and 0.06 mM were 54.71, 23.04, and 46.74 ns, which are much shorter than that (80.14 ns) of the pristine perovskite (x = 0). This result suggests that the incorporated CdS and $Cd(SCN_2H_4)_2Cl_2$ are beneficial to charge extraction and transfer at the TiO_2/C:C:$CH_3NH_3PbI_3$ (x) interface. Excessive doping (x = 0.06 mM) may slow down the interfacial charge transfer due to the insulation of the complex, thus leading to longer τ compared with the film with optimal doping concentration (x = 0.03 mM). Furthermore, the result indicates that the FTO/cp-TiO_2/mp-TiO_2/C:C:$CH_3NH_3PbI_3$ (0.03 mM) film has the shortest charge lifetime, indicating that the optimal doping concentration is 0.03 mM.

Fig. 4(a) shows the J–V characteristics of the FTO/cp-TiO_2/mp-TiO_2/$CH_3NH_3PbI_3$/spiro-OMeTAD/Au and FTO/cp-TiO_2/mp-TiO_2/C:C:$CH_3NH_3PbI_3$ (x)/spiro-OMeTAD/Au solar cells under AM 1.5G irradiation (100 mW·m^{-2}). The corresponding device parameters, including open circuit

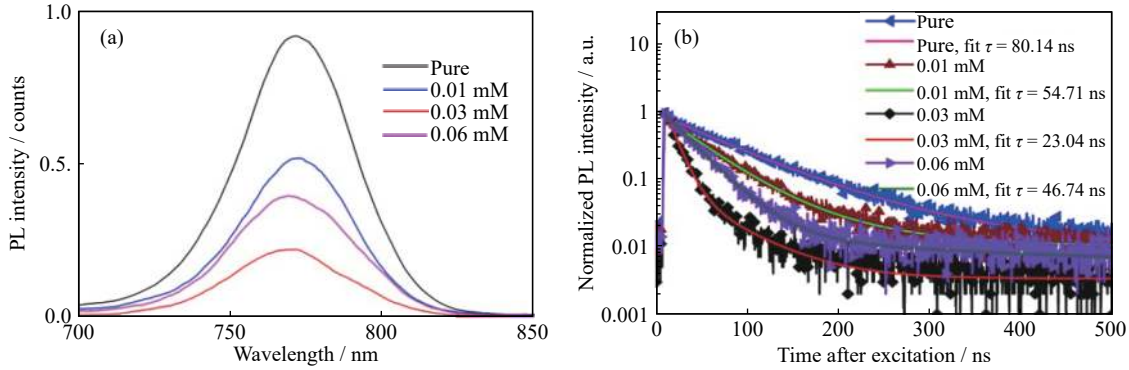

Fig. 3. (a) Photoluminescence spectra of FTO/cp-TiO_2/mp-TiO_2/$CH_3NH_3PbI_3$ and FTO/cp-TiO_2/mp-TiO_2/C:C:$CH_3NH_3PbI_3$ (x) films excited at 515 nm. (b) Time-resolved PL spectra of FTO/cp-TiO_2/mp-TiO_2/C:C:$CH_3NH_3PbI_3$ (x).

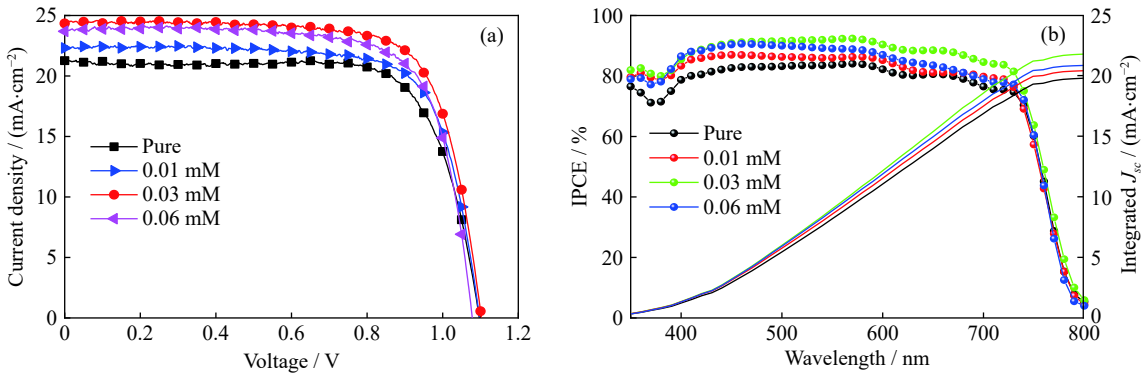

Fig. 4. (a) *J*–*V* characteristics and (b) measured IPCE spectra and integrated current density of PSCs based on C:C:$CH_3NH_3PbI_3$ (*x* = 0, 0.01, 0.03, and 0.06 mM) films under simulated AM 1.5G solar irradiation.

voltage (V_{oc}), short circuit current density (J_{sc}), fill factor (FF), and PCE, are summarized in Table 1. The difference between the V_{oc} of these cells was not obvious, whereas the J_{sc} of the cell with the C:C:$CH_3NH_3PbI_3$ (*x*) film was obviously higher than that of the cell with pristine $CH_3NH_3PbI_3$. Among all these cells, the cells of C:C:$CH_3NH_3PbI_3$ (0.03 mM) had the highest FF. Thus, given the high J_{sc} and FF, the cell based on the C:C:$CH_3NH_3PbI_3$ (0.03 mM) film had the highest PCE of 20.10% ± 0.3%, with an V_{oc} of 1.10 V, a J_{sc} of (24.34 ± 0.44) mA·cm^{-2}, and a FF of 0.75.

Fig. 4(b) shows the IPCE of the as-prepared cells. Results showed that the cells with CdS and $Cd(SCN_2H_4)_2Cl_2$ had a stronger IPCE response than the cell with only pristine $CH_3NH_3PbI_3$ in the whole wavelength range of 350–800 nm, suggesting more efficient charge separation and transport carrier accumulation in the C:C:$CH_3NH_3PbI_3$ (*x*) active layer. For each type of PSC, the integrated current density (J_{in}) obtained by integrating IPCE is also shown in Table 1, which agrees well with the measured J_{sc}. Furthermore, the cell with *x* = 0.03 mM exhibited the highest IPCE, suggesting a better charge extraction and less nonradiative charge recombination in the FTO/cp-TiO_2/mp-TiO_2/C:C:$CH_3NH_3PbI_3$ (0.03 mM)/spiro-OMeTAD/Au cell, as also proven by the hysteresis index (HI):

$HI = (PCE_{RS} - PCE_{FS})/PCE_{RS}$,

where PCE_{RS} refers to the efficiency of reverse scan, and PCE_{FS} refers to the efficiency of forward scan. As depicted in Table 1, when *x* = 0.03 mM, the optimized cell showed the minimum HI, which decreased from 3.00% of the control cell to 2.28%.

The dependence of V_{oc} and ln(J_{sc}) on the logarithm of light intensity ln(*I*) was measured to investigate the effect of incorporated CdS and $Cd(SCN_2H_4)_2Cl_2$ on charge recombination and transport kinetics. As shown in Fig. 5(a), the V_{oc} of the cells with four concentrations increased with increasing light intensity. When the incorporated concentrations *x* were 0, 0.01, 0.03, and 0.06 mM, the slopes were 1.16*kT*/*e*, 1.34*kT*/*e*, 1.09*kT*/*e*, and 1.81*kT*/*e*, respectively, where *K* is the Boltzmann constant, *T* is temperature, *e* is the electric charge. In general, the closer the slope is to 1*kT*/*e*, indicating that the main type of charge recombination is non-radioactive charge recombination rather than defect state-assisted charge recombination, the fewer defect states in the perovskite films. In particular, the slope of the cell with C:C:$CH_3NH_3PbI_3$ (0.03 mM) was the closest to 1*kT*/*e*. As illustrated in Fig. 5(a), the defect states in the perovskite crystal can be effectively reduced by doping CdS and $Cd(SCN_2H_4)_2Cl_2$ within the appropriate concentration.

Fig. 5(b) shows that the measured ln(J_{sc}) varied with the ln(*I*). The slope (1.00) for the device with C:C:$CH_3NH_3PbI_3$ (0.03 mM) was closer to 1 compared with those of other devices, suggesting less bimolecular charge recombination. The defect state density (n_{trap}) was also studied by the space charge limited current (SCLC) in the dark, and the result is displayed in Fig. 5(c). As the bias voltage was increased, the defects in the PSCs were filled by the injected charges, and when the bias voltage exceeded the trap-filling limit voltage (V_{TFL}), the current density increased quickly. Then, V_{TFL} can be obtained from the point of intersection, and the defect state density can be further estimated using the equation of $n_{trap} = 2\varepsilon_0\varepsilon V_{TFL}/(eL^2)$ [41–42], where ε_0 is the vacuum permittivity (ε_0 = 8.854 × 10^{-12} F·m^{-1}), ε is the dielectric constant of

Table 1. Performance parameters under simulated AM 1.5G solar irradiation

PSCs	V_{oc} / V	J_{sc} / (mA·cm^{-2})	J_{in} / (mA·cm^{-2})	FF	PCE / %	HI / %
Pure FS	1.10 ± 0.02	21.27 ± 0.52	20.10 ± 0.02	0.74 ± 0.05	17.31 ± 0.7	3.00
Pure RS	1.08 ± 0.02	21.03 ± 0.69	20.10 ± 0.02	0.73 ± 0.06	16.79 ± 1.1	
0.01 mM FS	1.10 ± 0.01	22.31 ± 0.49	20.70 ± 0.03	0.74 ± 0.02	18.16 ± 0.4	7.04
0.01 mM RS	1.09 ± 0.01	22.12 ± 0.31	20.70 ± 0.03	0.70 ± 0.03	16.88 ± 0.5	
0.03 mM FS	1.10 ± 0.01	24.34 ± 0.44	22.11 ± 0.01	0.75 ± 0.02	20.10 ± 0.3	2.28
0.03 mM RS	1.09 ± 0.01	24.19 ± 0.31	22.11 ± 0.01	0.74 ± 0.04	19.64 ± 0.6	
0.06 mM FS	1.08 ± 0.01	23.69 ± 0.61	21.10 ± 0.03	0.73 ± 0.02	18.68 ± 0.7	14.29
0.06 mM RS	1.05 ± 0.02	23.10 ± 0.54	21.10 ± 0.03	0.66 ± 0.03	16.01 ± 1.2	

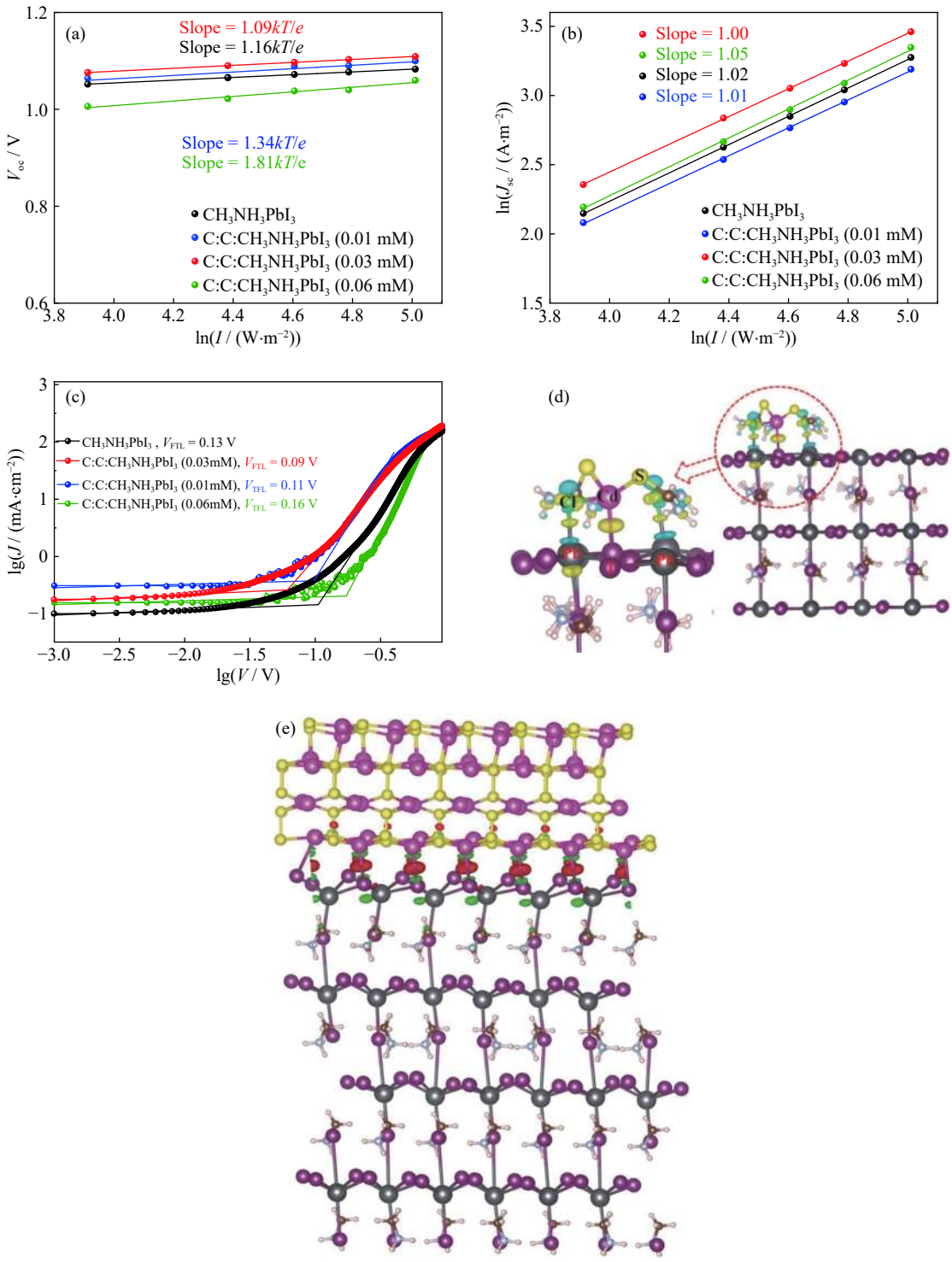

Fig. 5. (a) V_{oc} and (b) J_{sc} versus light intensity (50, 80, 100, 120, and 150 mW·cm^{-1}) for devices with different concentrations. (c) J–V characteristics of devices utilized for estimating the defect density for the cells. (d) Interfacial atom interaction at the interface of PbI_2 of $CH_3NH_3PbI_3$ in contact with the complex $Cd(SCN_2H_4)_2Cl_2$. (e) Atomic interaction between CdS and $CH_3NH_3PbI_3$ interface.

$CH_3NH_3PbI_3$ (ε = 32), e is the elementary charge (e = 1.6 × 10^{-19} C), and L is the thickness of the perovskite layer. For the device with pristine perovskite, the V_{TFL} was 0.13 V. After incorporating CdS and $Cd(SCN_2H_4)_2Cl_2$, as the concentration x increased from 0.01, 0.03, to 0.06 mM, the V_{TFL} initially decreased to 0.09 V and then increased to 0.16 V. The calculated results show that the n_{trap} values corresponding to x = 0, 0.01, 0.03, and 0.06 mM were 1.52 × 10^{15}, 1.28 × 10^{15}, 1.05 × 10^{15}, and 1.87 × 10^{15} cm^{-3}, respectively. Therefore, the device treated with C:C:$CH_3NH_3PbI_3$ (0.03 mM) had the fewest traps. When −3 < lg(V) < −2, the slope of lg(J)–lg(V) curves was very small. This phenomenon is mainly due to the existence of a large number of defect states in perovskite films because these defects can capture charge carriers injected by an external circuit, resulting in the slow increase in current.

The interaction between atoms at the $Cd(SCN_2H_4)_2Cl_2$/$CH_3NH_3PbI_3$ interface was analyzed by first-principles calculations to further explain the decrease in the defect density.

The calculation results in Fig. 5(d) show that the Cl and Cd atoms in $Cd(SCN_2H_4)_2Cl_2$ formed Cl−Pb and Cd−I chemical bonds with Pb and I atoms in the perovskite at the $Cd(SCN_2H_4)_2Cl_2/CH_3NH_3PbI_3$ interface, respectively. Thus, $Cd(SCN_2H_4)_2Cl_2$ can effectively reduce the defects caused by the unsaturated coordination of Pb atoms and the lack of I atoms in the $CH_3NH_3PbI_3$ crystals. Moreover, the atomic interaction at the $CdS/CH_3NH_3PbI_3$ interface is illustrated in Fig. 5(e). Results revealed that CdS could also reduce the defects caused by I atom deletion through the strong interaction between cadmium and iodine atoms in perovskite [36].

Furthermore, the $J^{1/2}$–V curves of PSCs are shown in Fig. 6(a) to investigate the effect of incorporated C:C on the electron mobility of perovskite film. The electron mobility μ_e in the perovskite film can be estimated by the SCLC model through the equation $J = 9\varepsilon_0\varepsilon_r\mu_e V^2/(8L^3)$ [17], where ε_r is the dielectric constant, μ_e is the electron mobility, V is the effective applied voltage, and L is the thickness of the function layer. The calculated μ_e values were 1.64×10^{-3}, 1.72×10^{-4}, 2.03×10^{-3}, and 1.42×10^{-3} $cm^2 \cdot V^{-1} \cdot s^{-1}$ for x = 0, 0.01, 0.03, and 0.06 mM, respectively. Obviously, the optimum doping concentration x is 0.03 mM.

The EIS of the $FTO/cp\text{-}TiO_2/mp\text{-}TiO_2/C{:}C{:}CH_3NH_3PbI_3$ (x)/spiro-OMeTAD/Au cells under AM 1.5G irradiation (100 $mW \cdot cm^{-2}$) was tested to study how the incorporated CdS and $Cd(SCN_2H_4)_2Cl_2$ affect the device performance. The obtained experimental results are shown in Fig. 6(b). An equivalent circuit was used to fit the experimental data to analyze the effect of the incorporated CdS and $Cd(SCN_2H_4)_2Cl_2$ on the charge recombination in the cells [43−44], as shown in the inset of Fig. 6(b). The fitting parameters are presented in Table 2. For the solar cells, the R_s is the ohmic series resistance, including the sheet resistance of the cp-TiO_2 layer, the spiro-OMeTAD layer, and the $CH_3NH_3PbI_3$ (or $C{:}C{:}CH_3NH_3PbI_3$) resistance. The left semicircle in high frequency region refers to the R_{HTM} for the resistance of the spiro-OMeTAD layer, and the right semicircle in the low frequency region refers to the R_{rec} for the charge recombination in the cells. C_{HTM} and C_μ are the capacitance of hole transport materials at the HTL/perovskite layer interface and the chemical capacitance of the cell, respectively. Results showed that R_{rec} initially increased and then decreased with increased x (from 0 to 0.06 mM). When x = 0.03 mM, R_{rec} reached the maximum value, suggesting that the charge recombination in the $FTO/cp\text{-}TiO_2/mp\text{-}TiO_2/C{:}C{:}CH_3NH_3PbI_3$ (x)/spiro-OMeTAD/Au cell is the least among all PSCs. Therefore, EIS results showed that the incorporated CdS and $Cd(SCN_2H_4)_2Cl_2$ effectively reduced the charge recombination in the PSCs, which suppressed charge recombination due to the decreased defect trap at perovskite grain boundaries.

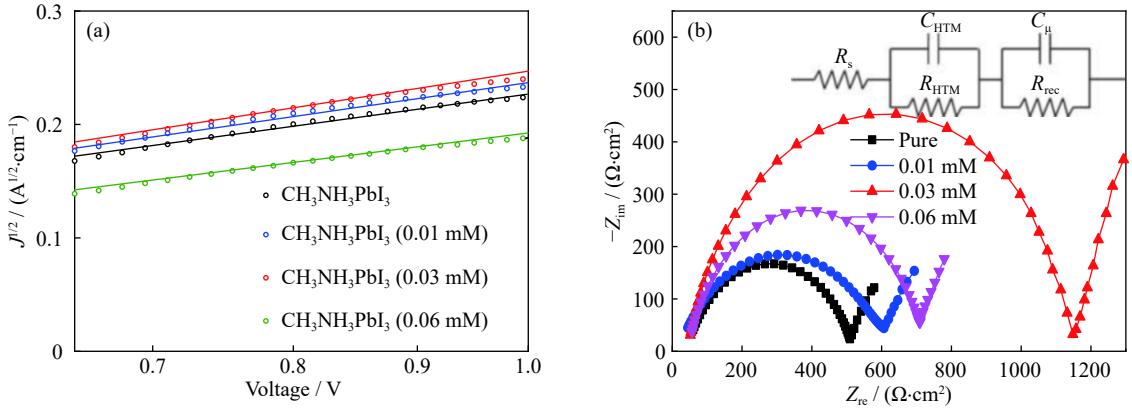

Fig. 6. (a) $J^{1/2}$–V curves of SCLC to calculate electron mobility. (b) EIS of PSCs under AM 1.5G irradiation (100 $mW \cdot cm^{-2}$) (x = 0.01, 0.03, and 0.06 mM). Insert: An equivalent circuit.

Table 2. Fitting parameters for measured EIS results with different devices

Device	R_s / ($\Omega \cdot cm^2$)	R_{HTM} / ($mA \cdot cm^{-2}$)	R_{rec} / ($mA \cdot cm^{-2}$)	C_{HTM} / ($\mu F \cdot cm^{-2}$)	C_μ / ($nF \cdot m^{-2}$)
Pure	47.32	476.5	529.7	32.04	51.45
0.01 mM	41.24	548.3	571.5	38.34	68.43
0.03 mM	34.59	109.3	116.9	47.96	73.78
0.06 mM	38.62	692.3	850.8	43.47	72.33

The long-term stability of the $FTO/cp\text{-}TiO_2/mp\text{-}TiO_2/C{:}C{:}CH_3NH_3PbI_3$ (x)/spiro-OMeTAD/Au cells with different incorporation concentrations of CdS and $Cd(SCN_2H_4)_2Cl_2$ were tested in ambient air (RH = 40%−50%) without encapsulation. As shown in Fig. 7, the PSCs without CdS and $Cd(SCN_2H_4)_2Cl_2$ only maintained 23.4% of the initial PCE value after 240 h, whereas the optimized cells with CdS (0.03 mM) and $Cd(SCN_2H_4)_2Cl_2$ treatment maintained 86.2% of the initial PCE value. For cells with other concentrations (0.01 and 0.06 mM), the retained PCE values were 38.1% and 51.0%, respectively. Compared with that of the PSCs within pristine $CH_3NH_3PbI_3$, the stability of the PSCs based on the $C{:}C{:}CH_3NH_3PbI_3$ perovskite layer showed great improvement, indicating that the $C{:}C{:}CH_3NH_3PbI_3$ composite

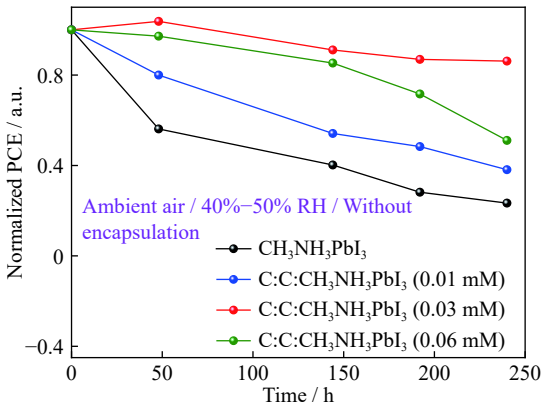

Fig. 7. Normalized PCE retentions of the cells based on $CH_3NH_3PbI_3$ and C:C:$CH_3NH_3PbI_3$ under ambient air without encapsulation.

film can slow the penetration of moisture and oxygen into the perovskite active layer. This result can be ascribed to the enlarged perovskite grains and the enhanced compactness of the C:C:$CH_3NH_3PbI_3$ composite film. The reduction of defects in the perovskite crystals may be another factor that improved the stability of the cell. In addition, when x = 0.06 mM, the stability of the PSCs dropped sharply. Excessive C:C doping possibly decreased the charge transfer efficiency in the perovskite active layer because of the poor conductivity of the complex.

4. Conclusion

We synthesized FTO/cp-TiO_2/mp-TiO_2/C:C:$CH_3NH_3PbI_3$/spiro-OMeTAD/Au solar cells with different CdS and $Cd(SCN_2H_4)_2Cl_2$ incorporation amounts and investigated the influence of CdS and $Cd(SCN_2H_4)_2Cl_2$ on the device performance. Results demonstrated that the incorporation of CdS and $Cd(SCN_2H_4)_2Cl_2$ could improve the compactness of the C:C:$CH_3NH_3PbI_3$ layer and the quality of perovskite film but did not alter the thickness of the perovskite layer. In addition, the charge transfer became more effective between the perovskite layer and the transport layers after the incorporation of CdS and $Cd(SCN_2H_4)_2Cl_2$, and the doping decreased the contact resistances at the C:C:$CH_3NH_3PbI_3$/HTL and C:C:$CH_3NH_3PbI_3$/ETL interfaces. This phenomenon led to an effective charge extraction from the perovskite layer to these two transport layers and thus reduced the charge recombination in the solar cells, thereby improving device performance.

Acknowledgements

This work was financially supported by the National Science Foundation for Young Scientists of China (No. 61704048), the Program for Science & Technology Innovation Talents in Universities of Henan Province, China (No. 19HASTIT049), the Key Research Project of Henan Provincial Higher Education, China (No. 19A140007), and the Natural Science Foundation for Young Scientists of Henan Province, China (No. 202300410060).

Conflict of Interest

The authors declare no conflict of interest.

References

[1] W.J. Yin, J.H. Yang, J. Kang, Y.F. Yan, and S.H. Wei, Halide perovskite materials for solar cells: A theoretical review, *J. Mater. Chem. A*, 3(2015), No. 17, p. 8926.

[2] C.B. Fei, B. Li, R. Zhang, H.Y. Fu, J.J. Tian, and G.Z. Cao, Highly efficient and stable perovskite solar cells based on monolithically grained $CH_3NH_3PbI_3$ film, *Adv. Energy Mater.*, 7(2017), No. 9, art. No. 1602017.

[3] X.X. Gao, W. Luo, Y. Zhang, R.Y. Hu, B. Zhang, A. Züttel, Y.Q. Feng, and M.K. Nazeeruddin, Stable and high-efficiency methylammonium-free perovskite solar cells, *Adv. Mater.*, 32(2020), No. 9, art. No. 1905502.

[4] H.B. Lee, N. Kumar, M.M. Ovhal, Y.J. Kim, Y.M. Song, and J.W. Kang, Dopant-free, amorphous-crystalline heterophase SnO_2 electron transport bilayer enables >20% efficiency in triple-cation perovskite solar cells, *Adv. Funct. Mater.*, 30(2020), No. 24, art. No. 2001559.

[5] Q. Lou, H.L. Li, Q.S. Huang, Z.T. Shen, F.M. Li, Q. Du, M.Q. Jin, and C. Chen, Multifunctional CNT:TiO_2 additives in spiro-OMeTAD layer for highly efficient and stable perovskite solar cells, *EcoMat*, 3(2021), No. 3, art. No. e12099.

[6] C.Q. Ma and N.G. Park, A realistic methodology for 30% efficient perovskite solar cells, *Chem*, 6(2020), No. 6, p. 1254.

[7] H. Min, D.Y. Lee, J.Kim, G. Kim, K.S. Lee, J. Kim, M.J. Paik, Y.K. Kim, K.S. Kim, M.G. Kim, T.J. Shin, and S. Il Seok, Perovskite solar cells with atomically coherent interlayers on SnO_2 electrodes, *Nature*, 598(2021), No. 7881, p. 444.

[8] G.H. Ren, W.B. Han, Y.Y. Deng, W. Wu, Z.W. Li, J.X. Guo, H.C. Bao, C.Y. Liu, and W.B. Guo, Strategies of modifying spiro-OMeTAD materials for perovskite solar cells: A review, *J. Mater. Chem. A*, 9(2021), No. 8, p. 4589.

[9] A. Kojima, K. Teshima, Y. Shirai, and T. Miyasaka, Organometal halide perovskites as visible-light sensitizers for photovoltaic cells, *J. Am. Chem. Soc.*, 131(2009), No. 17, p. 6050.

[10] S.D. Stranks, G.E. Eperon, G. Grancini, C. Menelaou, M.J.P. Alcocer, T. Leijtens, L.M. Herz, A. Petrozza, and H.J. Snaith, Electron-hole diffusion lengths exceeding 1 micrometer in an organometal trihalide perovskite absorber, *Science*, 342(2013), No. 6156, p. 341.

[11] J.L. Yang, K.M. Fransishyn, and T.L. Kelly, Comparing the effect of mesoporous and planar metal oxides on the stability of methylammonium lead iodide thin films, *Chem. Mater.*, 28(2016), No. 20, p. 7344.

[12] Y. Zhao, Q.F. Ye, Z.M. Chu, F. Gao, X.W. Zhang, and J.B. You, Recent progress in high-efficiency planar-structure perovskite solar cells, *Energy Environ. Mater.*, 2(2019), No. 2, p. 93.

[13] H.Y. Zhang, R. Li, W.W. Liu, M. Zhang, and M. Guo, Research progress in lead-less or lead-free three-dimensional perovskite absorber materials for solar cells, *Int. J. Miner. Metall. Mater.*, 26(2019), No. 4, p. 387.

[14] H. Lu, W. Tian, B.K. Gu, Y.Y. Zhu, and L. Li, TiO_2 electron transport bilayer for highly efficient planar perovskite solar cell, *Small*, 13(2017), No. 38, art. No. 1701535.

[15] F. Shahvaranfard, M. Altomare, Y. Hou, S. Hejazi, W. Meng, B. Osuagwu, N. Li, C.J. Brabec, and P. Schmuki, Engineering of the electron transport layer/perovskite interface in solar cells designed on TiO_2 rutile nanorods, *Adv. Funct. Mater.*, 30(2020), No. 10, art. No. 1909738.

[16] J.S. Manser, M.I. Saidaminov, J.A. Christians, O.M. Bakr, and

P.V. Kamat, Making and breaking of lead halide perovskites, *Acc. Chem. Res.*, 49(2016), No. 2, p. 330.
[17] G.J.A.H. Wetzelaer, M. Scheepers, A.M. Sempere, C. Momblona, J. Ávila, and H.J. Bolink, Trap-assisted non-radiative recombination in organic-inorganic perovskite solar cells, *Adv. Mater.*, 27(2015), No. 11, p. 1837.
[18] W.J. Yin, T.T. Shi, and Y.F. Yan, Unusual defect physics in $CH_3NH_3PbI_3$ perovskite solar cell absorber, *Appl. Phys. Lett.*, 104(2014), No. 6, art. No. 063903.
[19] H.P. Zhou, Q. Chen, G. Li, S. Luo, T.B. Song, H.S. Duan, Z.R. Hong, J.B. You, Y.S. Liu, Y. Yang, Interface engineering of highly efficient perovskitesolar cells, *Sci.*, 345(2014), No. 6196, p. 542.
[20] W.X. Gong, H. Guo, H.Y. Zhang, J. Yang, H.Y. Chen, L.P. Wang, F. Hao, and X.B. Niu, Chlorine-doped SnO_2 hydrophobic surfaces for large grain perovskite solar cells, *J. Mater. Chem. C*, 8(2020), No. 33, p. 11638.
[21] Q. Lou, G. Lou, R.X. Peng, Z.P. Liu, W. Wang, M.X. Ji, C. Chen, X.L. Zhang, C. Liu, and Z.Y. Ge, Synergistic effect of lewis base polymers and graphene in enhancing the efficiency of perovskite solar cells, *ACS Appl. Energy Mater.*, 4(2021), No. 4, p. 3928.
[22] J.K. Wang, K. Datta, C.H.L. Weijtens, M.M. Wienk, and R.A.J. Janssen, Insights into fullerene passivation of SnO_2 electron transport layers in perovskite solar cells, *Adv. Funct. Mater.*, 29(2019), No. 46, art. No. 1905883.
[23] S. Sonmezoglu and S. Akin, Suppression of the interface-dependent nonradiative recombination by using 2-methylbenzimidazole as interlayer for highly efficient and stable perovskite solar cells, *Nano Energy*, 76(2020), art. No. 105127.
[24] H.M. Yi, D. Wang, M.A. Mahmud, F. Haque, M.B. Upama, C. Xu, L.P. Duan, and A. Uddin, Bilayer SnO_2 as electron transport layer for highly efficient perovskite solar cells, *ACS Appl. Energy. Mater*, 1(2018), No. 11, p. 6027.
[25] J.J. Yan, Z.C. Lin, Q.B. Cai, X.N. Wen, and C. Mu, Choline chloride-modified SnO_2 achieving high output voltage in $MAPbI_3$ perovskite solar cells, *ACS Appl. Energy Mater*, 3(2020), No. 4, p. 3504.
[26] H.M. Yates, S.M.P. Meroni, D. Raptis, J.L. Hodgkinson, and T.M. Watson, Flame assisted chemical vapour deposition NiO hole transport layers for mesoporous carbon perovskite cells, *J. Mater. Chem. C*, 7(2019), No. 42, p. 13235.
[27] C. Chen, Y. Zhai, F.M. Li, F.R. Tan, G.T. Yue, W.F. Zhang, and M.T. Wang, High efficiency $CH_3NH_3PbI_3$:CdS perovskite solar cells with $CuInS_2$ as the hole transporting layer, *J. Power Sources*, 341(2017), p. 396.
[28] M. Samiee, S. Konduri, B. Ganapathy, R. Kottokkaran, H.A. Abbas, A. Kitahara, P. Joshi, L. Zhang, M. Noack, and V. Dalal, Defect density and dielectric constant in perovskite solar cells, *Appl. Phys. Lett.*, 105(2014), No. 15, art. No. 153502.
[29] M.X. Guo, F.M. Li, L.Y. Ling, and C. Chen, Electrochemical and atomic force microscopy investigations of the effect of CdS on the local electrical properties of $CH_3NH_3PbI_3$: CdS perovskite solar cells, *J. Mater. Chem. C*, 5(2017), No. 46, p. 12112.
[30] G. Kresse and J. Hafner, Ab initio molecular dynamics for liquid metals, *Phys. Rev. B*, 47(1993), No. 1, p. 558.
[31] G. Kresse and J. Furthmüller, Efficient iterative schemes for *ab initio* total-energy calculations using a plane-wave basis set, *Phys. Rev. B*, 54(1996), No. 16, p. 11169.
[32] . P. E. Blöchl, Projector augmented-wave method. *Phys. Rev. B*, 1994, *50*, 17953.
[33] H.J. Monkhorst and J.D. Pack, Special points for Brillouin-zone integrations, *Phys. Rev. B*, 13(1976), No. 12, p. 5188.
[34] S. Grimme, Semiempirical GGA-type density functional constructed with a long-range dispersion correction, *J. Comput. Chem.*, 27(2006), No. 15, p. 1787.
[35] K. Momma and F. Izumi, VESTA 3 for three-dimensional visualization of crystal, volumetric and morphology data, *J. Appl. Crystallogr.*, 44(2011), No. 6, p. 1272.
[36] L.X. Zhu, C. Chen, F.M. Li, Z.T. Shen, Y.J. Weng, Q.S. Huang, and M.T. Wang, Enhancing the efficiency and stability of perovskite solar cells by incorporating CdS and $Cd(SCN_2H_4)_2Cl_2$ into the $CH_3NH_3PbI_3$ active layer, *J. Mater. Chem. A*, 7(2019), No. 3, p. 1124.
[37] T.Y. Wang, B. Daiber, J.M. Frost, S.A. Mann, E.C. Garnett, A. Walsh, and B. Ehrler, Indirect to direct bandgap transition in methylammonium lead halide perovskite, *Energy Environ. Sci.*, 10(2017), No. 2, p. 509.
[38] N.K. Noel, A. Abate, S.D. Stranks, E.S. Parrott, V.M. Burlakov, A. Goriely, and H.J. Snaith, Enhanced photoluminescence and solar cell performance via lewis base passivation of organic–inorganic lead halide perovskites, *ACS Nano*, 8(2014), No. 10, p. 9815.
[39] H.R. Tan, A. Jain, O. Voznyy, X.Z. Lan, F.P. García de Arquer, J.Z. Fan, R. Quintero-Bermudez, M.J. Yuan, B. Zhang, Y.C. Zhao, F.J. Fan, P.C. Li, L.N. Quan, Y.B. Zhao, Z.H. Lu, Z.Y. Yang, S. Hoogland, and E.H. Sargent, Efficient and stable solution-processed planar perovskite solar cells via contact passivation, *Sci.*, 355(2017), No. 6326, p. 722.
[40] M.B. Johnston and L.M. Herz, Hybrid perovskites for photovoltaics: Charge-carrier recombination, diffusion, and radiative efficiencies, *Acc. Chem. Res.*, 49(2016), No. 1, p. 146.
[41] G. Tumen-Ulzii, C.J. Qin, T. Matsushima, M.R. Leyden, U. Balijipalli, D. Klotz, and C. Adachi, Understanding the degradation of spiro-OMeTAD-based perovskite solar cells at high temperature, *Sol. RRL*, 4(2020), No. 10, art. No. 2000305.
[42] Y.Q. Yang, J.H. Wu, X.P. Liu, Q.Y. Guo, X.B. Wang, L. Liu, Y. Ding, S.Y. Dai, and J.Y. Lin, Dual functional doping of $KMnO_4$ in spiro-OMeTAD for highly effective planar perovskite solar cells, *ACS Appl. Energy Mater.*, 2(2019), No. 3, p. 2188.
[43] J.A. Christians, R.C. Fung, and P.V. Kamat, An inorganic hole conductor for organo-lead halide perovskite solar cells. Improved hole conductivity with copper iodide, *J. Am. Chem. Soc.*, 136(2014), No. 2, p. 758.
[44] H.S. Kim, J.W. Lee, N. Yantara, P.P. Boix, S.A. Kulkarni, S. Mhaisalkar, M. Grätzel, and N.G. Park, High efficiency solid-state sensitized solar cell-based on submicrometer rutile TiO_2 nanorod and $CH_3NH_3PbI_3$ perovskite sensitizer, *Nano Lett.*, 13(2013), No. 6, p. 2412.